Journal of Computational Physics 228 (2009) 1294–1311

Contents lists available at ScienceDirect

Journal of Computational Physics

journal homepage: www.elsevier.com/locate/jcp

Vertically nested nonhydrostatic model for multiscale resolution of flows in the upper troposphere and lower stratosphere

Alex Mahalov *, Mohamed Moustaoui

Center for Environmental Fluid Dynamics, Department of Mechanical and Aerospace Engineering, Department of Mathematics and Statistics, Arizona State University, Tempe, AZ 85287-1804, USA

ARTICLE INFO

Article history:
Received 10 April 2008
Received in revised form 2 October 2008
Accepted 13 October 2008
Available online 7 November 2008

PACS:
65M06
65M12
76E06
76R10
76U05
86A10

Keywords:
Nonhydrostatic atmospheric model
Vertical nesting
Multiscale flows in the upper troposphere and lower stratosphere

ABSTRACT

Vertical nesting with refined gridding in coupled mesoscale weather research and forecasting (WRF)/microscale models are presented with a particular emphasis on improved vertical resolution in the upper troposphere and lower stratosphere (UTLS). The finest mesoscale nest is coupled with a sequence of microscale nests with finer resolution in both the horizontal and the vertical. The fully three-dimensional, compressible nonhydrostatic Navier–Stokes equations are solved using a time-split method with a refined grid in the vertical, and improved resolution in the UTLS region. For nesting, both lateral and vertical boundary conditions are treated via implicit relaxation in buffer zones where all fields are relaxed to those obtained from the finest mesoscale nest. Computational results are presented demonstrating the ability of microscale nests to resolve multiscale physics of strongly nonlinear interactions and laminated structures observed in the Terrain-induced rotor experiment (T-REX) campaign of field measurements. Very high resolution real case nested simulations are conducted. The microscale nests fully resolve localized shear layers and sharp gradients of vertical velocity and potential temperature near the tropopause and in the lower stratosphere.

1. Introduction

Significant advances in computation of atmospheric flows have been achieved during the last decades. The dramatic increase in computer power has facilitated developments of nonhydrostatic mesoscale numerical weather prediction (NWP) codes that have capabilities to resolve small-scale atmospheric processes. This was achieved by implementation of nesting techniques with multiple domains resolving horizontal scales ranging from few to hundreds kilometers, and by the improvement of sub-grid scale parameterizations. Among these models, the advanced research version of the weather research and forecasting model (WRF–ARW) is a next generation mesoscale NWP model [1]. It is the first fully compressible conservative-form nonhydrostatic atmospheric model suitable for both research and weather prediction applications. The WRF–ARW model represents the latest developments following a particular modeling approach that uses time-splitting techniques to efficiently integrate the fully compressible nonhydrostatic equations of motion. The integration scheme uses a time-split method to circumvent the acoustic-mode time step restriction, where the meteorologically significant modes are integrated

* Corresponding author.
E-mail addresses: mahalov@asu.edu (A. Mahalov), mousta66@pearson.la.asu.edu (M. Moustaoui).

0021-9991/$ - see front matter © 2008 Elsevier Inc. All rights reserved.
doi:10.1016/j.jcp.2008.10.030

by using a third-order Runge–Kutta (RK) scheme. The spatial discretization typically uses a fifth-order differences for advection, and the vertical coordinate is based on Terrain following hydrostatic pressure coordinate.

There are two main techniques that are used in atmospheric and oceanic models to improve resolution over limited areas. In dynamically adaptive methods, the spatial resolution is constantly changing with time by coarsening or refining the grid spacing depending on local conditions [19,20]. The adaptive methods are not well established in the atmospheric modeling systems for several reasons [21]: (i) adaptive techniques can incur massive overhead due to indirect data addressing and additional efforts for grid handling which increase the cost of real time forecasting; (ii) physical parameterizations of sub-grid processes are usually optimized for a specific grid resolution, making it difficult to use dynamically and temporally refined or coarsened grids. The other method uses nesting to improve spatial resolution over a limited area. Nesting are widely used in atmospheric (i.e. MM5 [22], WRF [1], COAMPS [23]) and oceanic (i.e. ROMS [24]) models. Large domain models with coarse resolution are used to predict large-scale dynamics, while limited area models with boundary conditions interpolated from coarse grids are used over small domains with finer resolution. The improvement allowed by nesting techniques is that small-scale processes which are not resolved in a coarse grid model, and therefore need to be represented by using sub-grid-scale parameterizations, may be explicitly resolved in the nested model.

One of the main difficulties faced in atmospheric as well as oceanic nested modeling is the specification of the lateral boundary conditions. Usually, the prognostic fields at the lateral boundaries of the nested grid are specified from the large domain. These fields have coarse resolution, and are interpolated in space and time to the nested grid. The inconsistencies between the limited and the large domain solutions create spurious reflections that may propagate and affect the solution in the interior of the nested domain. Several approaches are used to handle the lateral boundary conditions. The flow relaxation scheme [4,5] is the most frequently used for atmospheric mesoscale forecasting models over a limited domain. Lateral open boundary conditions are often used in limited area ocean modeling. These conditions include radiation condition, combined radiation and prescribed condition depending on the inflow and outflow regime at the boundary, and a scale selective approach. A review of these methods is given in [25].

Nesting options are implemented in WRF–ARW. Nevertheless, as in many nonhydrostatic mesoscale atmospheric models, nesting is allowed only in the horizontal direction and all nests use the same grid distribution in the vertical. For real applications, NWP models still use a limited number of grid points in the vertical that is typically well below 100. Usually, grid stretching is implemented to increase the vertical resolution in the boundary layer and lower levels at the expense of the upper troposphere and lower stratosphere (UTLS). The extended region consisting of the bulk of the troposphere and the lower stratosphere represents a significant challenge for numerical prediction. The collusion between the stratification and shear in the UTLS region leads to many complex multiscale physics phenomena, including the formation of vertically thin, laminated structures [15,13]. The lack of vertical resolution in the UTLS region may present a severe limitation in resolving small-vertical-scale processes such as clear air turbulence patches and thin adiabatic layers characterized by sharp vertical gradients at the edges. They are observed in the UTLS region during extreme events such as wave breaking, overshooting moist convection, shear-instabilities near jet streams and gravity wave-critical level interactions [17,16]. These small scale upper level processes are particularly sensitive to the vertical resolution, implying that the vertical grid spacing typically used in operational models is likely insufficient to resolve these vertical scales. NWP systems employ a range of parameterizations to model the effects of unresolved sub-grid processes on the large-scale dynamics. Resolving explicitly these small-scale processes requires computations using fine mesh in both the vertical and the horizontal to encompass all pertinent multiscale phenomena in the UTLS region. This, coupled with sharp velocity and temperature gradient profiles, presents significant challenges for nesting.

In this paper, we treat the computational aspects of physical problems with a particular emphasis on improved vertical resolution of atmospheric flows near the tropopause and in the lower stratosphere. We present for the first time high resolution coupled WRF–ARW/microscale system, where the microscale domains are nested both in the horizontal and the vertical, and where all microscale fields are relaxed towards the WRF finest nest. We present a new relaxation method based on the flow relaxation scheme, where the relaxation is implemented as an implicit correction in the acoustic time step, and we show examples demonstrating that this method is very effective and robust. Computational results in real atmospheric conditions are presented demonstrating the ability of microscale nests to resolve multiscale physics of strongly nonlinear laminated structures observed in the UTLS region. The paper is organized as follows: the model formulation and the computational approach are presented in Section 2. The performance of the model is shown in Section 3. The ability of microscale nests to resolve laminated structures observed in the UTLS region is demonstrated in Section 4, where our computational methodology is applied to the field data obtained during the Terrain-induced rotor experiment (T-REX). Finally summary and conclusion are given in Section 5.

2. Model formulation and computational approach

Our coupled WRF with microscale vertical nesting model simulations are produced by conducting mesoscale simulations with several nests interacting in a two way mode, with a finest WRF nest that uses a horizontal grid spacing of 1 km. The number of vertical sigma pressure levels used for these nests is 150, and they are adjusted to achieve an improved resolution near the tropopause and in the lower stratosphere. The pressure at the top is $p_{top} = 10$ mb, and the vertical resolution is about $\delta z = 150$ m in the UTLS region. WRF simulations are initialized with high resolution global data, that is the European

Centre for Medium-Range Weather Forecasts (ECMWF) analysis with the spectral truncation T799L91. These data have a resolution that uses a horizontal grid spacing of 25 km and are distributed on 91 vertical levels.

Vertical nesting is implemented by coupling the finest resolution nest of WRF with a sequence of microscale nests. The microscale nests are constructed with increased resolution in both the horizontal and the vertical, with refined vertical gridding to resolve small-scales processes near the tropopause and in the lower stratosphere ($\delta z = 50$ m). We use implicit relaxation for both upper and lateral boundary conditions. The microscale fields are relaxed within relaxation zones to the finest WRF nest fields including the vertical velocity. The WRF fields are interpolated in time and space in these relaxation zones. The vertically relaxed upper boundary conditions prevent the formation of spurious wave reflection at the top of the domain. WRF code run first, the output of the finest grid mesoscale nest is used as a coarse grid input for the microscale nest. In the real case simulations presented in this study, the WRF fields are archived with a frequency of 30 min. WRF outputs are interpolated in time, in the horizontal and in the vertical, to provide initial and boundary conditions for the microscale code, and finally, the microscale nest run is made alone.

We use the WRF model as a base to develop the microscale code. This code solves the 3D fully compressible nonhydrostatic Navier–Stokes equations for atmospheric dynamics. To insure consistency with WRF, these equations are cast in conservative form and are formulated using a Terrain-following pressure coordinate [2] denoted by η and defined as: $\eta = (p_{dh} - p_{dht})/\mu_d$ where $\mu_d = p_{dhs} - p_{dht}$, and μ_d represents the mass of the dry air in the column and p_{dh}, p_{dht} and p_{dhs} represent the hydrostatic pressure of the dry atmosphere and the hydrostatic pressure at the top and the surface of the dry atmosphere. The formulated moist equations are:

$$\partial_t U + (\nabla \cdot \mathbf{V}u)_\eta + (\alpha/\alpha_d)(\alpha_d \partial_x p + \partial_\eta p \partial_x \phi) = F_U, \tag{1}$$

$$\partial_t V + (\nabla \cdot \mathbf{V}v)_\eta + (\alpha/\alpha_d)(\alpha_d \partial_y p + \partial_\eta p \partial_y \phi) = F_V, \tag{2}$$

$$\partial_t W + (\nabla \cdot \mathbf{V}w)_\eta - g[(\alpha/\alpha_d)\partial_\eta p - \mu_d] = F_W, \tag{3}$$

$$\partial_t \Theta + (\nabla \cdot \mathbf{V}\theta)_\eta = F_\theta, \tag{4}$$

$$\partial_t \mu_d + (\nabla \cdot \mathbf{V})_\eta = 0, \tag{5}$$

$$\partial_t \phi + \mu_d^{-1}[(\mathbf{V} \cdot \nabla \phi)_\eta - gW] = 0, \tag{6}$$

$$\partial_t Q_m + (\nabla \cdot \mathbf{V}q_m)_\eta = F_{Q_m}. \tag{7}$$

In these equations, $\mathbf{v}$ (u, v, w) is the physical velocity vector, θ is the potential temperature, p is the pressure, g is the acceleration of gravity and $\phi = gz$ is the geopotential. $(U, V, W, \Omega, \Theta) = \mu_d(u, v, w, \omega, \theta)$, where $\omega = d\eta/dt$ is the vertical velocity in the computational space, and $\mathbf{V} = (U, V, \Omega)$ is the coupled velocity vector. The right-hand-side terms F_U, F_V, F_W, and F_θ represent forcing terms arising from model physics, turbulent mixing, spherical projections, and the earth's rotation.

The above governing equations are solved together with the diagnostic equation for coupled dry inverse density,

$$\partial_\eta \phi = -\alpha_d \tag{8}$$

and the diagnostic relation for the full pressure (vapor plus dry air) $p = p_0(R_d \Theta_m / p_0 \alpha_d)^\gamma$. In these equations, α_d is the coupled inverse density of the dry air (μ_d/ρ_d) and α is the coupled inverse density taking into account the full parcel density $\alpha = \alpha_d(1 + q_v + q_c + q_r + q_i + \cdots)^{-1}$ where $q_\star$ are the mixing ratios (mass per mass of dry air) for water vapor, cloud, rain, ice, etc. Additionally, $\Theta_m = \Theta(1 + (R_v/R_d)q_v) \approx \Theta(1 + 1.61 q_v)$, and $Q_m = \mu_d q_m; q_m = q_v, q_c, q_i, \ldots$

The main difference between the Eqs. (1)–(8) and those solved in WRF is the use of a coupled inverse density α_d and α rather than the inverse density as in WRF [1]. This results in a different formulation for the pressure gradient terms in the momentum equations, and in the acoustic time steps. The pressure gradient terms in the momentum equations have the following forms:

$$P_x = (\alpha/\alpha_d)(\alpha'_d \bar{p}_x + \alpha_d p'_x + \bar{\mu}\phi'_x + p'_\eta \phi_x),$$
$$P_y = (\alpha/\alpha_d)(\alpha'_d \bar{p}_y + \alpha_d p'_y + \bar{\mu}\phi'_y + p'_\eta \phi_y),$$
$$P_z = -g((\alpha/\alpha_d)p'_\eta - \mu' + (\alpha/\alpha_d - 1)\bar{\mu})$$

and Eq. (8) takes the form:

$$\partial_\eta \phi' = -\alpha'_d. \tag{9}$$

The prime variables indicate the deviation with respect to the reference state (i.e. $p' = p - \bar{p}$). The reference state has to depend on the altitude only, and must satisfy the hydrostatic balance for the above formulation to hold.

The details of the solver used are described in [1]. Here, we give a brief summary and we discuss the differences between our model and WRF. We use the time-split scheme developed in [3] as the basis for the integration scheme. In this method, low-frequency modes that are meteorologically significant are integrated using a third-order RK time integration scheme; while high-frequency acoustic modes are handled by using an implicit scheme in the vertical with smaller time steps to maintain stability. We note that the RK scheme used in Wicker and Skamarock [3] is implemented in a way that is different from the standard RK schemes. This scheme is easily implemented and it does not require the storage of all evaluated steps until the final step. It has many advantages compared with the leap-frog scheme which is used in other time-split

nonhydrostatic NWP models (MM5, COAMPS). It is more accurate, stable for both diffusion and advection equations and allows to use centered and upwind biased spatial discretizations. It does not require time filtering that degrades the accuracy of the solution as in the leap-frog scheme, where time filtering is necessary to damp the computational modes. The spatial discretization uses a C grid staggering: normal velocity are staggered one-half grid length from the thermodynamic variables. Advection of vector and scalar fields is in the form of flux divergence, The advection uses a fifth or a third-order accurate up-winded spatial discretization. As in WRF we use a technique that consists of integrating perturbation equations. In these equations, each variable ψ is decomposed as $\psi = \psi^t + \psi''$, where ψ^t is the most updated value in the RK step for ψ, and ψ'' is the perturbation with respect to this value.

In our formulation, the pressure gradient terms in the horizontal momentum perturbation equations have the form:

$$P''_x = (\alpha/\alpha_d)(\alpha''_d \bar{p}_x + \alpha_d p''_x + \bar{\mu}\phi''_x + p''_\eta \phi_x),$$
$$P''_y = (\alpha/\alpha_d)(\alpha''_d \bar{p}_y + \alpha_d p''_y + \bar{\mu}\phi''_y + p''_\eta \phi_y).$$

Eq. (9) becomes in the acoustic integration:

$$\partial_\eta \phi'' = -\alpha''_d \tag{10}$$

and the linearized form of the equation of state is given by:

$$p'' = p\gamma(\Theta''/\Theta - \alpha''/\alpha). \tag{11}$$

We found that by introducing a coupled inverse density, the number of arithmetic operations required for the pressure gradient evaluations in the horizontal momentum equations is reduced by 20%. We note that the linearized equation of state (11) does not include the mass of the dry air μ''.

For the initial state, WRF fields are interpolated horizontally; then the mesoscale fields are also interpolated in the vertical to adjusted levels that can be chosen independently from the WRF vertical levels. Our interpolation approach follows a class of high order monotone shape preserving schemes [12,18]. The interpolation used to redistribute the initial data on the finer grid is based on 1D shape preserving interpolation combining the Hermite cubic monotonic polynomial with the Akima derivative estimate modified to satisfy the sufficient condition for monotonicity [12]. This interpolation preserves monotonicity and avoids generation of numerical noise or local extrema. Once the fields are interpolated the coupled inverse density is calculated by using Eq. (8). We choose to compute this variable instead of interpolating it from WRF to ensure that (8) is satisfied for the initial conditions. This avoids generation of large transients at the initial time if (8) is not satisfied.

The reference state is constructed from the initial state by interpolating the thermodynamic fields from sigma to z-coordinate. These fields are averaged in the horizontal. The reference pressure profile is then calculated using the hydrostatic relation applied in z-coordinate together with the gas law. The reference vertical profile of the geopotential is obtained by re-interpolating the thermodynamic profiles to sigma coordinate, and using (8) so that the numerical formulation of the hydrostatic relation is satisfied.

The relaxation towards coarse grid fields is implemented using operator splitting method applied in the acoustic steps where a prognostic variable is updated first without any relaxation. The relaxation is applied as an implicit correction step after each acoustic step. The corrected variable is then used to update the other prognostic variables. We also use an implicit absorbing layer near the top of the domain [8].

For the lateral boundary conditions, the normal velocity component located at the boundary is treated differently from the tangential velocities and the thermodynamic variable which are located half grid point inside the domain and adjacent to the boundary. The relaxation boundary scheme consists of progressively constraining the main prognostic variables of the limited area model to match the corresponding values from the coarse grid model in a buffer zone next to the boundary called "relaxation" zone. The flow relaxation scheme used in this study is a combination of Newtonian and diffusive relaxation that have the form:

$$\partial_t \psi = -N(x)(\psi - \psi^c) + D(x)\partial_{xx}(\psi - \psi^c),$$

where ψ is a prognostic variable of the limited area model that needs to be relaxed to the corresponding variable from the coarse grid model ψ^c; x denotes the direction normal to the boundary, and $N(x)$ and $D(x)$ are the Newtonian and the diffusive relaxation factors. This form of relaxation was introduced in [4], and is widely used in limited area atmospheric models. The choice of the profiles and the values of the coefficients $N(x)$ and $D(x)$ in the relaxation zones control reflections at the boundary. They are discussed in [5–7].

In our model, the relaxation is implemented after each acoustic step as an implicit correction. Let $\tilde{\psi}''^{,n+1}$ denotes the perturbation of the updated variable after each acoustic time step. The relaxation is then applied as a correction in a subsequent step using the following implicit flow relaxation equation:

$$\frac{\psi''^{,n+1}_i - \tilde{\psi}''^{,n+1}_i}{\delta\tau} = -N_i(\psi''^{,n+1}_i + \psi^t_i - \psi^{c,n+1}_i) + \frac{D_i}{\delta x^2}\Big\{(\psi''^{,n+1}_{i+1} + \psi^t_{i+1} - \psi^{c,n+1}_{i+1}) - 2(\psi''^{,n+1}_i + \psi^t_i - \psi^{c,n+1}_i) + (\psi''^{,n+1}_{i-1} + \psi^t_{i-1} - \psi^{c,n+1}_{i-1})\Big\},$$

where $\delta\tau$ is the acoustic time step, δx is the grid spacing and $\psi^{c,n+1}_i$ is the coarse grid value interpolated in space and to the time step $(n+1)$. $\psi''^{,n+1}_i = \psi^{n+1}_i - \psi^t_i$, where ψ^{n+1}_i is the total fine grid value, ψ^t_i is the most updated value in the RK step and

$\psi_i''^{,n+1}$ is the perturbation with respect to ψ_i^t. For the prognostic variables located at half grid points adjacent to the lateral boundary, this implicit equation is solved for $\psi_i''^{,n+1}$ along the relaxation zone, subject to the boundary conditions:

$$\psi_{s+1}''^{,n+1} = \tilde{\psi}_{s+1}''^{,n+1} \text{ and } \psi_1''^{,n+1} = \psi_1^{c,n+1} - \psi_1^t,$$

where s is the index of the last relaxed point in the interior of the domain.

For the normal velocities at the boundary, the same system is solved except that we impose that the coarse and the limited area mass fluxes in the continuity Eq. (5) are consistent, that is:

$$\nabla \cdot \mathbf{V} = \nabla \cdot \mathbf{V^c},$$

where $\mathbf{V}$ and $\mathbf{V^c}$ are the velocity vectors from the limited area and the coarse grid models, coupled with the mass of the dry air per unit area within the column. Since the tangential velocities adjacent to the boundary are imposed by the coarse grid model, the above relation reduces to:

$$\frac{\partial U}{\partial x} = \frac{\partial U^c}{\partial x},$$

where U and U^c are the normal components of $\mathbf{V}$ and $\mathbf{V^c}$ respectively. This relation is imposed implicitly at the lateral boundaries, and the implicit equation is solved for $U''^{,n+1}$ along the relaxation zone as above, but with the following implicit boundary conditions:

$$U_{s+1}''^{,n+1} = \tilde{U}_{s+1}''^{,n+1} \text{ and } U_2''^{,n+1} - U_1''^{,n+1} = \left(U_1^t - U_1^{c,n+1}\right) - \left(U_2^t - U_2^{c,n+1}\right).$$

In the vertical, a constant pressure is imposed at the top of the domain. All the prognostic variables are computed by the model including at the top. After updating these variables in the acoustic step, the same relaxation is applied in a buffer zone near the top of the domain, except that the implicit Newtonian relaxation is used alone. The geopotential, however, is not relaxed in the vertical.

The Newtonian and diffusive relaxation times are fixed by the choice of the coefficients N_i and D_i. Optimal profiles for the Newtonian relaxation coefficient N are proposed in [5,6]. They are constructed in such a way that, under idealized conditions, the unwanted partial reflection of outgoing waves leaving the domain is minimized. More recently, [7] conducted a detailed theoretical and numerical study on the choice of the Newtonian and diffusive relaxation coefficients, where they compared different profiles and relaxation times. They concluded that a diffusive relaxation combined with exponential or optimized profiles gives better results. Also, they presented formula for what they called the leading coefficients $N_2^\star$ and $D_2^\star$ which they derived using the criterium of minimum reflection. These are nondimensional coefficients at the first relaxed grid point. These coefficients together with the relaxation profiles determine the entire relaxation time in the relaxation zone through the relations:

$$N_i = -\frac{c}{2\delta x} N_2^\star \widetilde{N}_i \text{ and } D_i = -\frac{c\delta x}{2} D_2^\star \widetilde{D}_i.$$

In these relations c is the phase speed of the fastest wave, and $\widetilde{N}_i$ and $\widetilde{D}_i$ are the normalized profiles of the coefficient ($\widetilde{N}_2 = 1$ and $\widetilde{D}_2 = 1$). In our implicit relaxation, we choose a nine-point deep relaxation zone where Newtonian and diffusive relaxation are applied. Following [7], we choose $N_2^\star = 0.9$ and $D_2^\star = 0.8$; c is the speed of sound, and an optimized profile is computed for $\widetilde{N}_i$ and $\widetilde{D}_i$ using the algorithm presented in [6]. These specifications determine entirely the Newtonian and diffusive relaxation times. The effectiveness and robustness of the proposed technique will be demonstrated in the next section.

Our numerical code is written in Fortan90 which facilitate its portability to different platforms. The code is fully parallelized using MPI, and the memory used by the code is optimized. The simulations conducted for these studies are performed on ASC MSRC SGI Altix "Eagle" platform (INTEL ITANIUM-II processors), NAVO MSRC IBM P5 "Babbage" platform, and HPC Intel Xeon cluster at Arizona State University (ASU).

3. Model performance and benchmarks

Several tests are conducted by comparing the model results in idealized dry and moist cases for which the behavior of the expected solution is documented in the literature. The benchmarks have been validated by other nonhydrostatic models. They include mountain waves, gravity current and squall-line developments in moist deep convection (see Appendix). In the following and in the supplementary discussion in Appendix, nesting in all presented idealized tests uses the microscale model alone. That is, coarse grid simulations are carried out using the microscale code; then outputs from these simulations are interpolated and used in the same code for limited area and fine grid computations. In the real case simulations, the microscale code is coupled to the WRF model. The parent and the nested domains use the same pressure at the top.

3.1. Test of the implicit relaxation

Simulations of mountain wave generation above an idealized topography are conducted to demonstrate the ability of the proposed relaxation technique to absorb gravity waves and to prevent wave reflection at the lateral boundary as well as at

the top of the domain. Waves are forced by a bell shaped mountain: $h(x) = \frac{h_0}{1+(x/L)^2}$, where $h_0 = 1$ km and $L = 80$ km is the half width. A large domain simulation is conducted using the model presented in Section 2. We use open lateral boundary conditions, and an implicit absorbing layer near the top of the domain presented recently in [8]. The large domain simulation uses a third-order advection in both the horizontal and the vertical, a time step $\delta t = 40$ s and 202 points in the horizontal with a grid spacing of $\delta x = 4$ km. The horizontal extent (unstaggered) of the domain is [−400 km, 400 km]. This test uses 60 points in the vertical, and the pressure imposed at the top is $p_{top} = 50$ mb. The initial wind is $u_0 = 10$ ms^{-1}. Outputs for the prognostic fields are archived every 100 time steps. To test the performance of the proposed lateral relaxation, the outputs are truncated within a limited area [−120 km, 120 km], and another simulation is conducted using the same model within this limited area without increasing the resolution. This simulation uses the same configuration as in the large domain (same δx and vertical grid distribution), except that the number of grid points in the horizontal is truncated to 62, and all prognostic fields are relaxed to the outputs from the large domain using the proposed method. The width of the relaxation zone is nine points. The coarse grid outputs are interpolated in time to provide the boundary conditions at intermediate times. Fig. 1(a) shows a cross-section for the vertical velocity after 1600 time steps from the large domain simulation, but plotted in the limited area only. Fig. 1(b) shows the same fields obtained from limited area simulation. In this case, the eastern and the western edges of the plot correspond to the actual lateral boundaries. Comparison between Fig. 1(a) and Fig. 1(b) demonstrates that the method proposed for the relaxation performs well. To compare this technique with the one used in many nonhydrostatic NWP models (i.e. WRF), we conducted two other limited area simulations using the same model as in Fig. 1(b), except that the relaxation is implemented as explicit tendency terms added to the rhs of (1)–(7) in the RK step. In this case, the relaxation zone uses five points and the coefficients are given by:

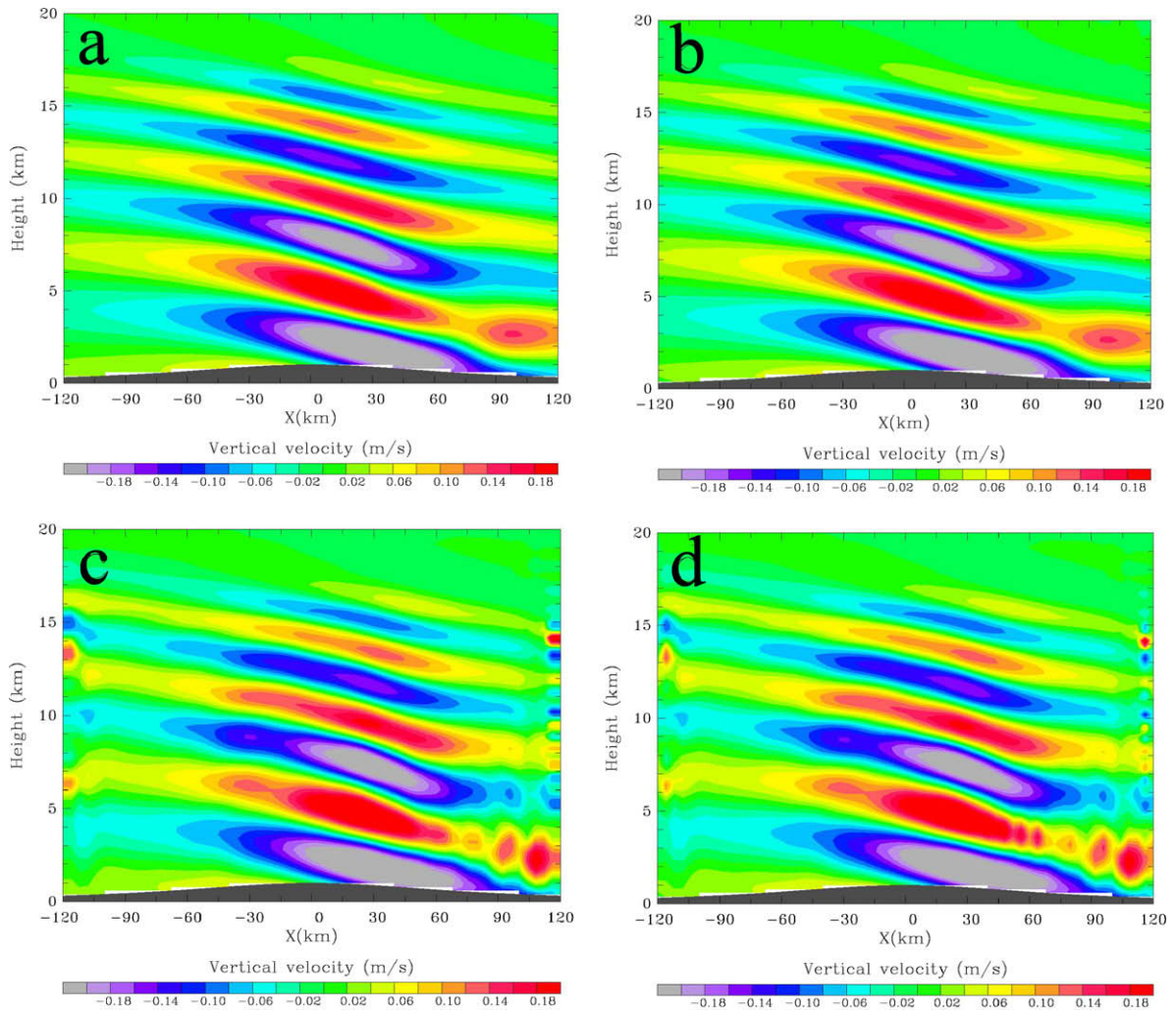

Fig. 1. Vertical cross-sections of vertical velocity after 1600 time steps from (a) large domain simulations, and from the limited area simulations using (b) the implicit relaxation, (c) explicit relaxation with zero-gradient for vertical velocity and (d) explicit relaxation for all fields.

$$N_i = \frac{1}{10\Delta t}\frac{5-i}{3} \quad \text{and} \quad D_i = \frac{\delta x^2}{50\Delta t}\frac{5-i}{3}.$$

Fig. 1(c) shows the cross-section for vertical velocity obtained by imposing a zero gradient for vertical velocity and by relaxing the other variables. Spurious reflections are found near the lateral boundaries. These reflections affect the solution in the interior of the limited area domain. Fig. 1(d) shows the cross-section for vertical velocity by relaxing all fields including the vertical velocity. Similar spurious reflections as in Fig. 1(c) are present. These reflections are absent when the relaxation is implemented as an implicit correction in the acoustic step using the proposed relaxation method (Fig. 1(b)). In this case, the solution is almost undistinguishable from the truncated large domain solution (Fig. 1(a)). Another simulation (not shown) was performed using the same explicit relaxation as in Fig. 1(d), except that the lateral profile for the relaxation zone uses nine points instead of five. The reflections near the boundary were not removed by this change. We also tested the implicit relaxation using five points instead of nine (not shown). In this case the reflections off the boundaries were strongly reduced. Thus, the key explanation for the removal of these reflections in Fig. 1(b) is the implicit treatment in the proposed method. We note that all the tests shown in Fig. 1 use the same large domain data for the lateral boundary conditions. For these simulations the large domain data are archived with the same frequency (each 100 steps). The results obtained by the proposed implicit relaxation method are superior (Fig. 1(b)). Fig. 1 shows that the technique used in this method is more effective and robust. It should be noted that when the large domain data are archived more frequently, the spurious reflections are reduced in Fig. 1(c) and (d).

To test the performance of the upper relaxation, two simulations are conducted. These simulations use the same configuration as in Fig. 1(b), except that the upper gravity wave absorbing layer is turned off for the limited area simulation. In one simulation the prognostic variables are relaxed in the lateral direction only. Fig. 2(a) shows the vertical velocity field plotted at the same time as in Fig. 1(b). Strong gravity wave reflections develop near the top of the domain. We note that these reflections were not present when the upper gravity wave absorbing layer presented in [8] was applied (Fig. 1(b)), indicating that this absorbing layer is very effective and robust. In a second simulation, the absorbing layer is also turned off, but all fields are relaxed near the top towards the large domain solution using the proposed implicit relaxation method. Fig. 2(b) shows the resulting cross-section. It should be noted that the results in Fig. 2(b) were obtained without any upper absorbing layer. The spurious reflections at the top are completely reduced compared to Fig. 2(a). The results compare very well with those in Fig. 1(b) where the relaxation is done in the horizontal with an absorbing layer near the top. Thus, the proposed implicit relaxation acts also as an effective absorbing layer when the large domain data are not contaminated by reflections at the top.

Fig. 3(a) shows potential temperature and vertical velocity for a real case test using the microscale code where all fields are relaxed to temporally and spatially interpolated fields from the finest WRF nest, in our coupled WRF mesoscale/microscale simulations of T-REX. In this case, the relaxation is implemented as a correction step. Fig. 3(b) shows the same field, but from a one way nest using WRF alone, after vertically interpolating all fields and using them again as inputs in WRF. The pressure at the top is 10 mb for both cases. These results will be described in details in Section 4. Here we only want to assess improvements in simulations using relaxation techniques for lateral boundary conditions. In Fig. 3(a) and (b), the cross section is taken within the relaxation zone at four grid points inside the domain from the southern lateral boundary. Fig. 3(c) shows the finest WRF fields used as coarse grid values in the relaxation zone. For comparison, the fields in Fig. 3(c) are plotted in the microscale domain only. It is clear from these figures that the spurious values of vertical velocity (Fig. 3(b)) are

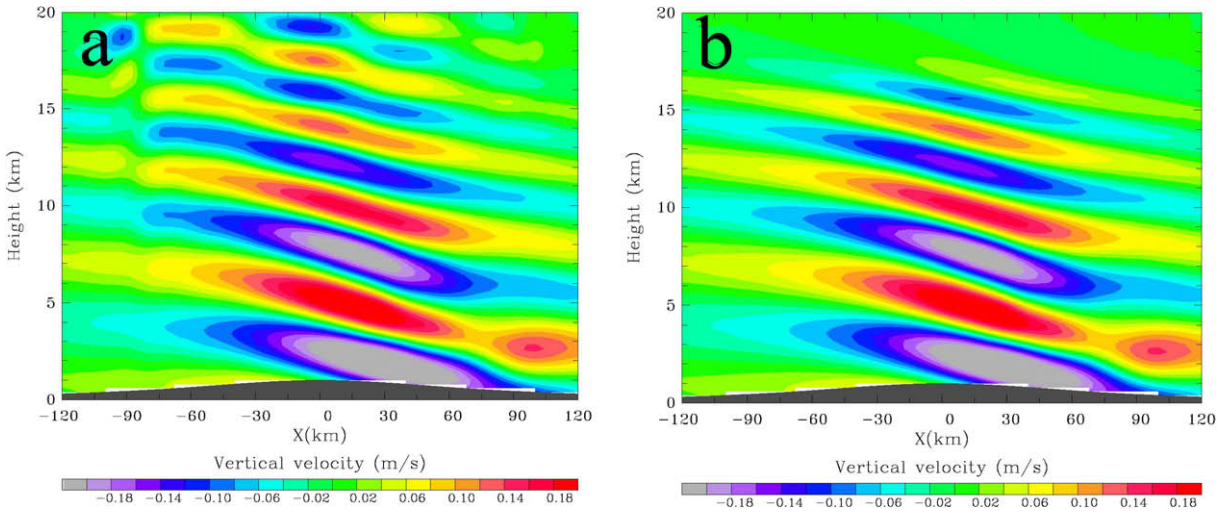

Fig. 2. Vertical cross-sections of vertical velocity after 1600 time steps from limited area simulations (a) without upper relaxation and (b) with upper relaxation.

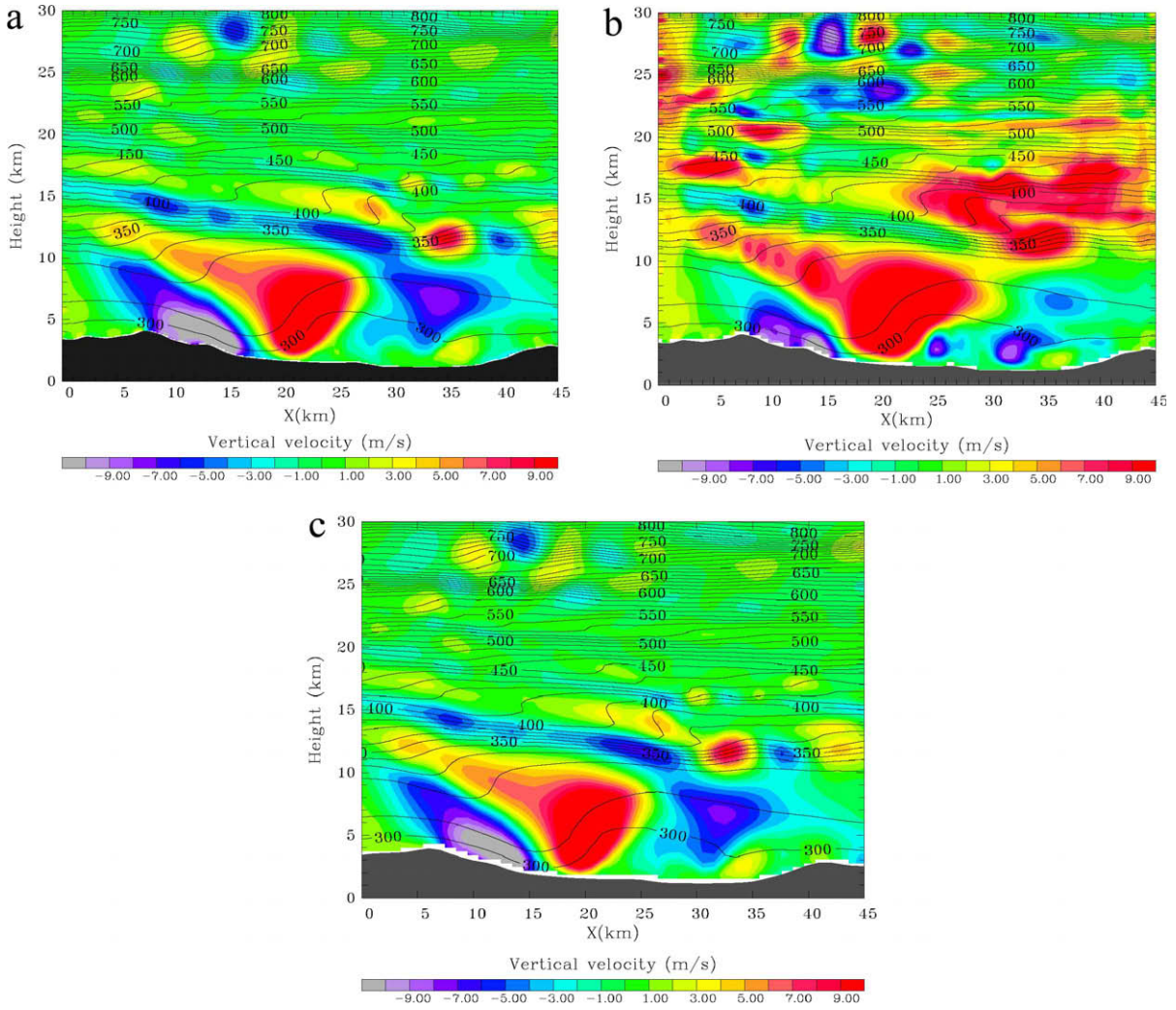

Fig. 3. Vertical cross-sections of potential temperature (contour) and vertical velocity (a): from microscale simulations using relaxation to the WRF finest nest, (b): from WRF using the same microscale domain as in (a), after vertically interpolating the finest WRF outputs and using them as inputs in WRF one way nesting and (c): from the WRF finest nest plotted in the microscale domain only. The time is April 1, 2006 at 8:00 UTC.

drastically reduced in the microscale code (Fig. 3(a)). These spurious values are higher near the eastern and the western boundaries, and affect the solution inside the domains as can be seen from Fig. 3(b).

Fig. 4 shows potential temperature and vertical velocities during T-REX for other two simulations using the microscale code where all the prognostic fields except the geopotential are relaxed in the vertical towards the finest WRF nest (Fig. 4(a)), and without any vertical relaxation (Fig. 4(b)). The nonrelaxed case develops strong spurious high velocities at the top of the domain. In the relaxed case, however, spurious values of vertical velocity do not develop. The vertical relaxation acts as an absorbing layer with respect to WRF results, and effectively reduces wave reflection at the top of the domain. It should be noted that, even if the coarse grid WRF or microscale fields do not include spurious reflections, spatial interpolation and, in particular finer topography in the nested model introduce dynamical imbalances which cause generation of transients. This is the case in WRF (Fig. 3(b)) and in the microscale model (Fig. 4(b)). The role of the relaxation is to reduce these transients.

4. Multiscale resolution of laminated structures in the upper troposphere and lower stratosphere (UTLS)

High resolution coupled WRF mesoscale/microscale code simulations for real atmospheric conditions are carried out to demonstrate the ability of our microscale nests to resolve small-scale processes in the UTLS region driven by nonhomogeneous shear and stratification associated with sharp vertical gradient in temperature and wind across the tropopause. Such multiscale stratospheric flows are characterized by patchy high frequency fluctuations in the wind fields and long-lived

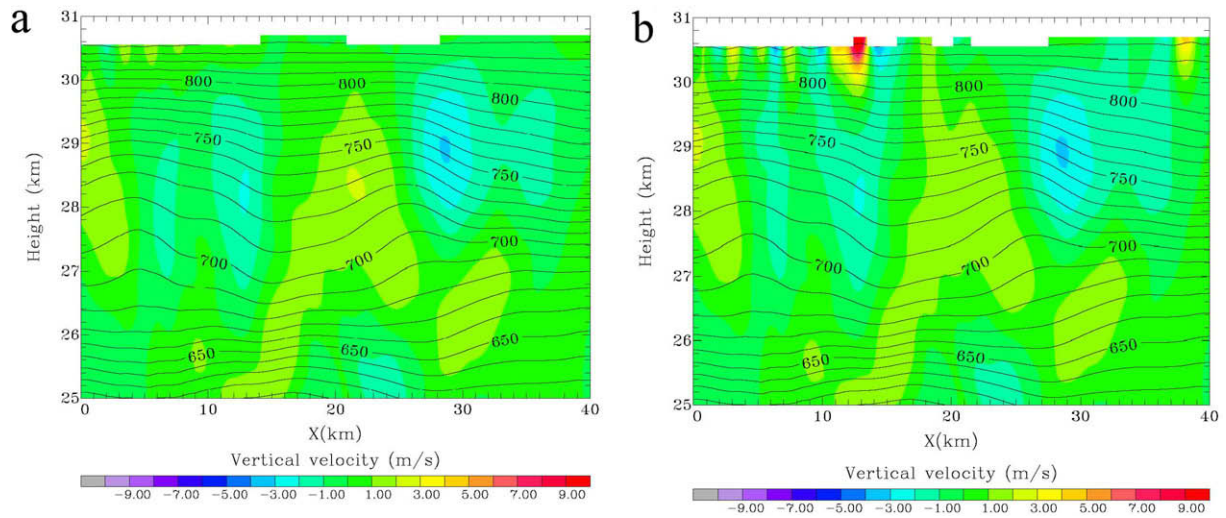

Fig. 4. Vertical cross-sections of potential temperature (contour) and vertical velocity near the top boundary from microscale simulations using (a) vertical relaxation of fields to the WRF finest nest and (b) without any vertical relaxation. The time is April 1, 2006 at 6:10 UTC.

energetic eddies with small-scales which are not resolved by even the latest generation of mesoscale meteorological models. Effective resolution and prediction of strongly nonlinear multiscale physical phenomena and laminated structures in the UTLS region is a significant challenge for real time operational forecasting.

The Terrain-induced rotor experiment (T-REX) campaign [14] represents an important benchmark for real case simulations of strongly nonlinear multiscale dynamics near the tropopause and in the lower stratosphere associated with high activity of topographic gravity waves. During this campaign, several radiosondes were launched from the upwind side of Owens Valley, CA. Owens Valley is located to the east of Sierra Nevada mountain. This mountain is nearly two-dimensional mountain range. It ranges 640 km long and 60–130 km wide, mostly in Eastern California. The ridge line of Sierra Nevada mountain rises to approximately 3500 m, and the tallest peak reaches 4, 418 m in Mt. Whitney, the highest peak in the United States outside Alaska. During the TREX campaign, vertical profiles of temperature and wind components were measured with high vertical resolution from the ground up to 30 km. Many profiles exhibit high temperature and wind wave-like fluctuations in the lower stratosphere, with different vertical wavelengths and localized adiabatic layers where potential temperature gradients are small. For instance, Fig. 5 (left panel) shows vertical profiles of potential temperature, eastward and northward wind components, from measurements during TREX performed by a balloon launched at (36.49 N, 118.84 W) on April 1, 2006 at 7:50 UTC. High level of activity of mountain waves is evident from these profiles. The potential temperature profile shows several regions above the tropopause (11 km) where the vertical gradients are small (i.e. 12 km, 14 km and 20 km). The vertical profile of the square of Brunt Vaisala frequency (Fig. 5 right panel) shows strong inhomogeneities near the tropopause. The Brunt Vaisala frequency (N) is a measure for stability, and is defined by $N^2 = (g/\theta)(\partial\theta/\partial z)$. Here, g is the constant of gravity, θ is the potential temperature, and z is the vertical coordinate. The Brunt Vaisala frequency experiences a sharp increase across the tropopause. In Fig. 5 we observe a significant increase in stability in a thin layer around 11.2 km with values reaching $N^2 = 19 \times 10^{-4}$ s^{-2} and exceeding those usually observed in the stratosphere ($N^2 = 4 \times 10^{-4}$ s^{-2}). Above this level, the stability decreases within thin adiabatic layers in the lower stratosphere; and increases again thereafter reaching a second maximum just below 13 km. This laminated structure with layering of local maxima and minima in stability was also observed in other profiles measured during TREX campaign. The structures present in these profiles exhibit high activity of mountain waves, with complex nonlinear dynamics involving small and large-scales processes as indicated in the profiles presented in Fig. 5. These profiles show coexistence of smaller and larger vertical wavelengths. Small-scale structures and thin mixed layers have also been observed in the upper troposphere and lower stratosphere above deep convection during other experiments [17,16]. Real case simulations with resolutions that are higher than those used in standard mesoscale codes are required to adequately resolve these thin adiabatic layers and localized maxima in stability near the tropopause and in the lower stratosphere. Vertical nesting is required to resolve nonlinear processes involving small-vertical-scales.

Our coupled mesoscale WRF with microscale vertical nests simulations are conducted for the period from 03/31/2006 00 UTC to 04/2/2006 00 UTC of the T-REX campaign of measurements. WRF domains are centered over (36.49 N, 118.8 W). Three mesoscale domains (Fig. 6(a)–(c)) are used with horizontal resolutions of 15 km, 3 km and 1 km, and 150 vertical sigma pressure levels from the ground up to 10 mb ($\sim$ 30 km altitude). These levels are adjusted for better resolution of the tropopause and the lower stratosphere. The grid spacing in the UTLS region is about $\delta z \sim 150$ m. Mesoscale WRF simulations are initialized with high resolution ECMWF T799L91 analysis data, 25 km horizontal resolution and 91 vertical levels.

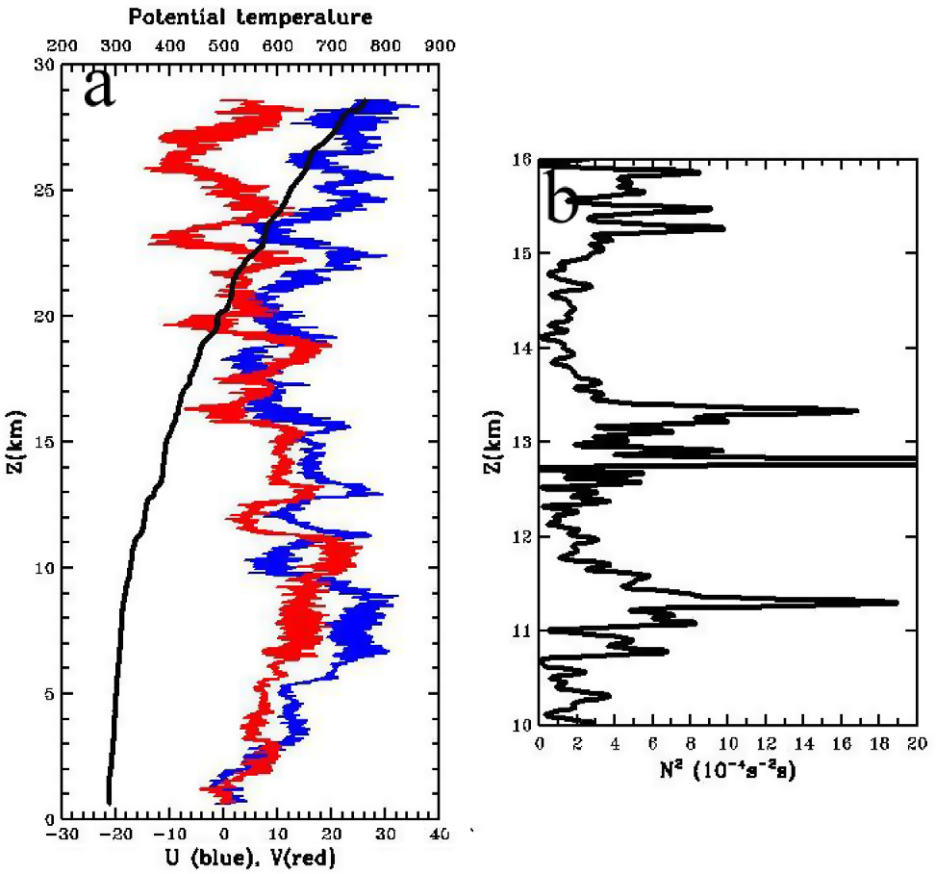

Fig. 5. Potential temperature (black), eastward wind (blue), and northward wind (red) from balloon measurements during T-REX. The balloon was launched at (36.49 N, 118.84 W) on April 1, 2006 at 7:50 UTC.

The miscroscale domain uses 300×300 in the horizontal and much higher vertical resolution with 450 staggered vertical levels, and a vertical grid spacing of $\delta z \sim 50$ m. It is nested both horizontally and vertically, with initial and boundary conditions from the finest WRF mesoscale domain. Fig. 6(d) shows topography for the microscale nest (100 km $\times$ 100 km horizontal dimensions). The black curve superimposed in Fig. 6 presents the trajectory of a balloon launched on April 1, 2006 at 7:50 UTC from the location (36.49 N, 118.84 W) in the upstream side of the highest elevation. During the ascent, the balloon drifts north-eastward, and is located on the downstream side of the highest elevation as it reaches levels above the tropopause (blue dot).[1] The wind vector field at $z = 12$ km from the microscale simulation on April 1, 2006 at 8:00 UTC is also superimposed in Fig. 6(d). The wind directions are dominated by south-westerlies in agreement with observations. We note that the relaxation of the wind field is very smooth at the boundaries. Regions with strong turbulent flow are well resolved in the microscale nest and are found above the valley, towards the south of the balloon trajectory. In these regions, the horizontal wind field shows strong drag, and the direction of the wind is complex.

Fig. 7 shows longitude (118.56 W, 117.42 W)–altitude cross-section at latitude 36.82 N for potential temperature (contour) and vertical velocity (color) on April 1, 2006 at 8:00 UTC from the microscale nest. These fields show clear evidence of mountain waves signature, with high activity primarily occurring in the downstream side of the mountain. The phase lines in potential temperature field exhibit rearward phase tilts that are characteristic of mountain waves. Regions with small-vertical gradients of potential temperature are found in the UTLS region as well as in the boundary layer. These adiabatic layers are associated with small-scale patches of high vertical velocity reaching 5–9 m s^{-1} in the UTLS.

In the microscale results (Fig. 7), we observe several localized thin layers above the tropopause where the potential temperature contours are well packed together indicating strong local increase in stability. These layers show a wave-like pattern with horizontal wavelengths as short as 5 km near $x = 40$ km. This wave is not excited directly by topography, since its wavelength is much smaller than the horizontal scale of the mountains, and because it is not observed in potential temperature field below 12 km at upper tropospheric levels (9–10 km). At some levels above 12 km, there are regions in the lower stratosphere where stratification decreases within adiabatic layers, while other regions show localized sharp gradients. The

[1] For interpretation of color in Figs. 1–6 and 9–12, the reader is referred to the web version of this article.

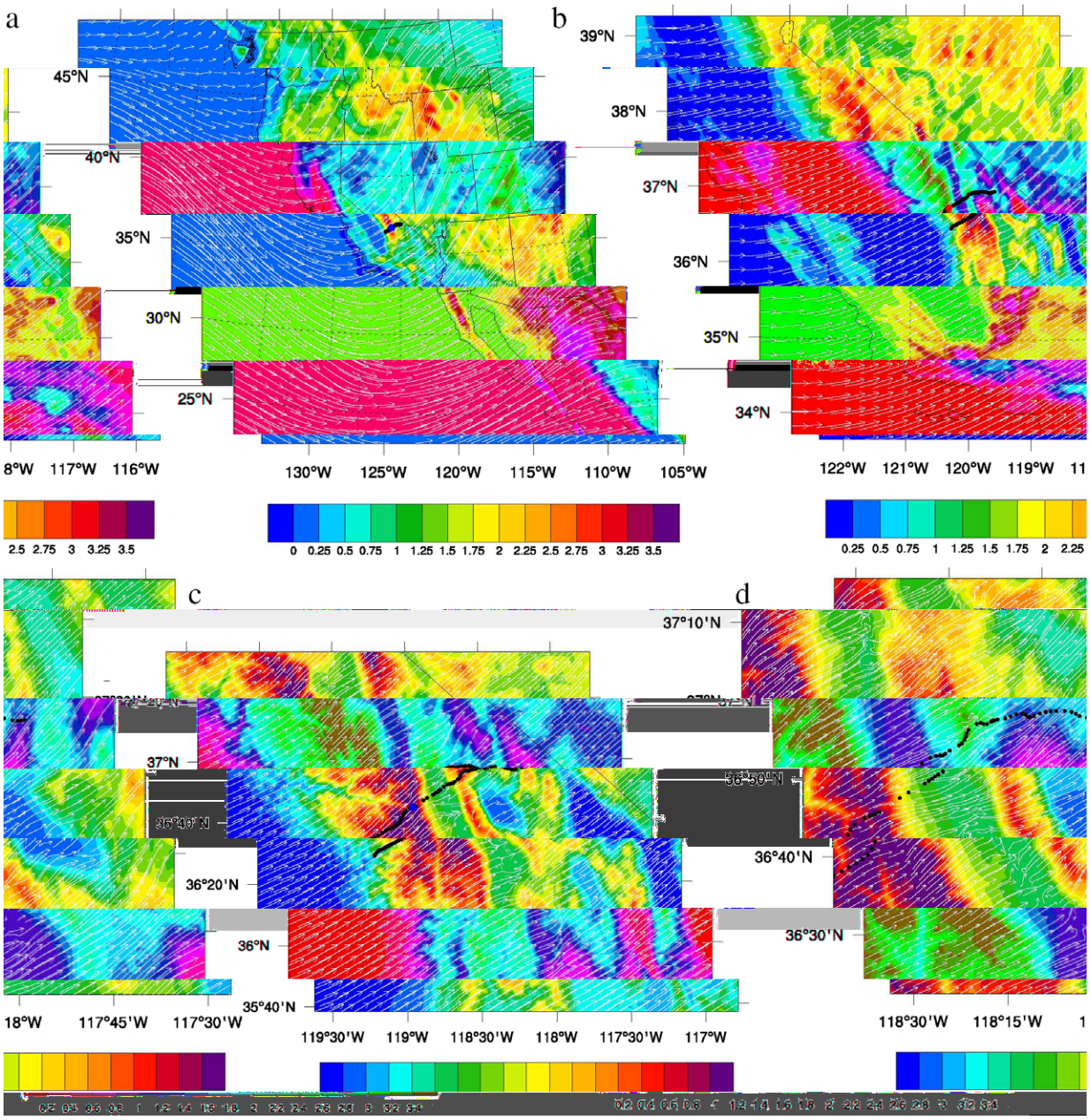

Fig. 6. Wind vector fields at 12 km and topography used for WRF domains (a) 15 km, (b) 3 km, (c) 1 km horizontal grid spacing and (d) for the microscale nest. The black curve shows the balloon trajectory. The time is April 1, 2006 at 8:00 UTC.

resulting strong local inhomogeneities in stratification with layering of local maxima and minima were observed during TREX campaign of measurements (Fig. 5).

Fig. 8(a)–(c) shows zooms of cross-sections for potential temperature and eastward wind in the UTLS region from WRF large domain ($\Delta x = 15$ km), the intermediate domain ($\Delta x = 3$ km) and the finest WRF nest ($\Delta x = 1$ km) respectively. Fig. 8(d) shows the fields obtained from the microscale nest for the same zoom. The potential temperature and the eastward velocity fields simulated by the microscale model exhibit multiscale structures with fine details that are not resolved in the mesoscale nests (Fig. 8(a)–(c)). We note from these figures that as the horizontal resolution increases, the structures present in the fields simulated by WRF mesoscale nests become better resolved. The microscale nest uses a finer grid in the vertical with 450 levels, and provides further improvement in resolution of fine laminated structures and patches of high vertical velocity in the UTLS region.

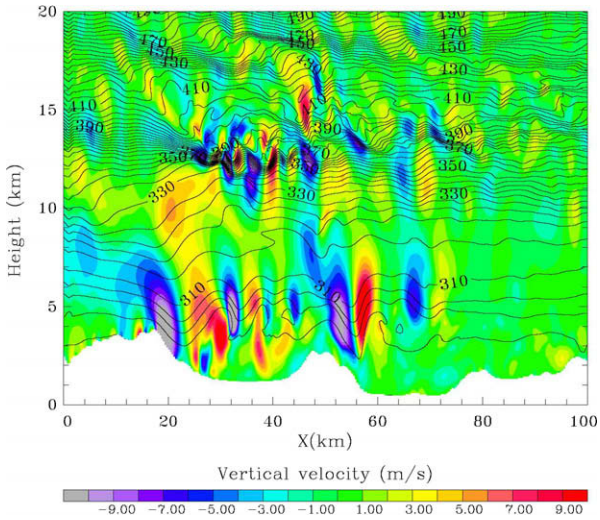

Fig. 7. Longitude–altitude cross-section for potential temperature and vertical velocity on April 1, 2006 at 8:00 UTC from the microscale nest.

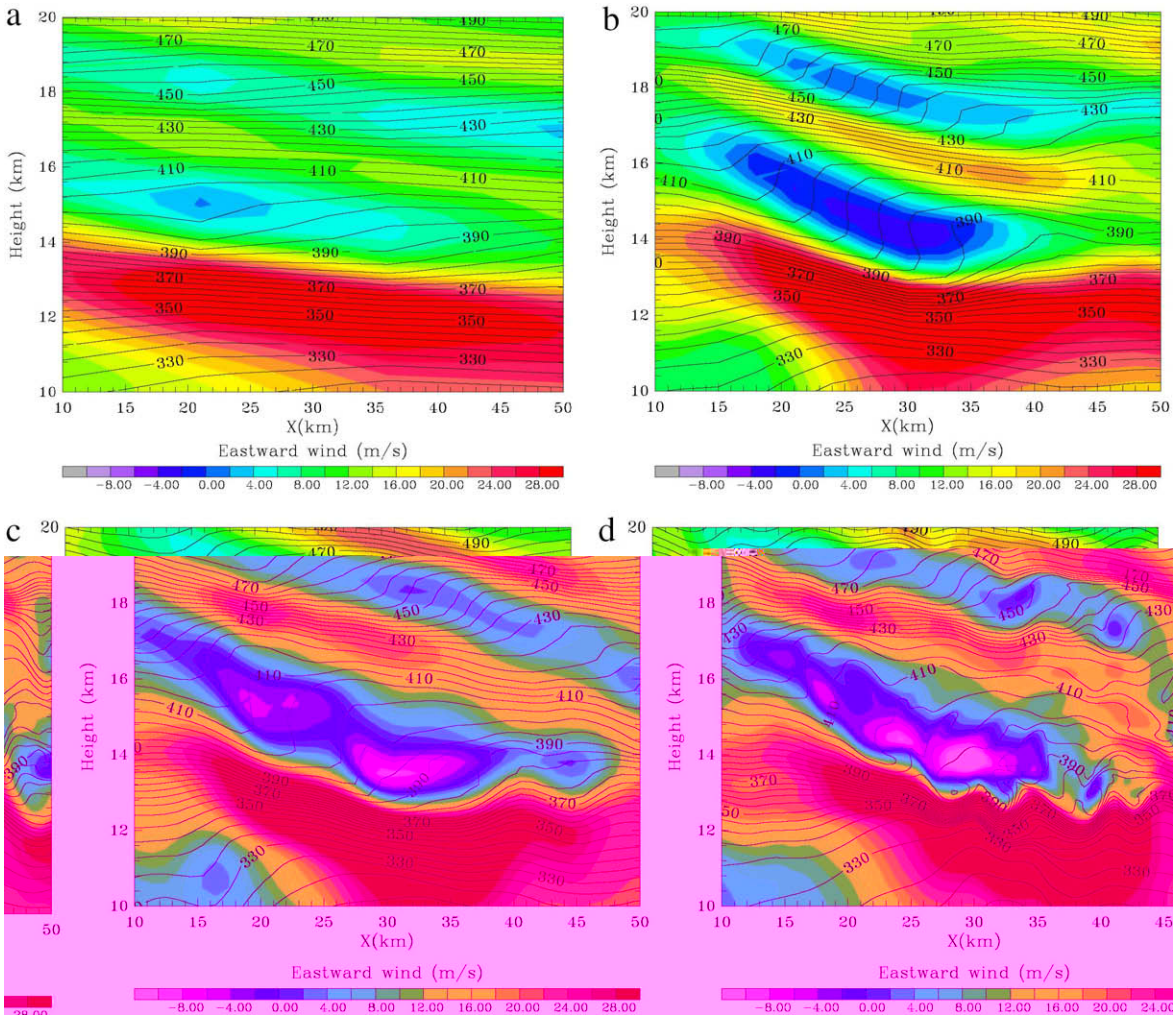

Fig. 8. Longitude–altitude cross-section for eastward velocity and potential temperature in the UTLS region (a) from 15 km WRF domain, (b) 3 km WRF domain, (c) 1 km WRF domain and (d) from the microscale nest. The time is April 1, 2006 at 8:00 UTC.

Fig. 9(a) and (b) show longitude–altitude cross-sections from the microscale simulations for Richardson number and the shear, respectively. The Richardson number is defined by $R_i = N^2/((\partial u/\partial z)^2 + (\partial v/\partial z)^2)$. R_i is used in shear stratified flows to identify regions where instabilities may develop ($R_i < 0.25$). In Fig. 9(a) and (b) patches of low Richardson number and strong shear are well resolved in the microscale nest, with finer details compared to the finest mesoscale simulations (Fig. 9(c) and (d)). They are found primarily below 5 km and at upper levels around the tropopause and in the lower stratosphere. Small-scales develop in the potential temperature and vertical velocity fields primarily in these regions (Fig. 7). These strongly mixed layers are induced by nonlinear interactions triggered by nonlinear rotor waves near the ground and by wave breaking and shear instabilities in the UTLS region. They are well resolved by vertical nesting in our microscale simulations.

Fig. 10 shows a zoom for potential temperature, eastward velocity and vertical velocity simulated by the microscale model. In the lower stratosphere, the formation of a layer with strong stratification is evidenced by well packed potential temperature contours. This layer is bounded above and below by regions with relatively small stratifications. It is modulated by

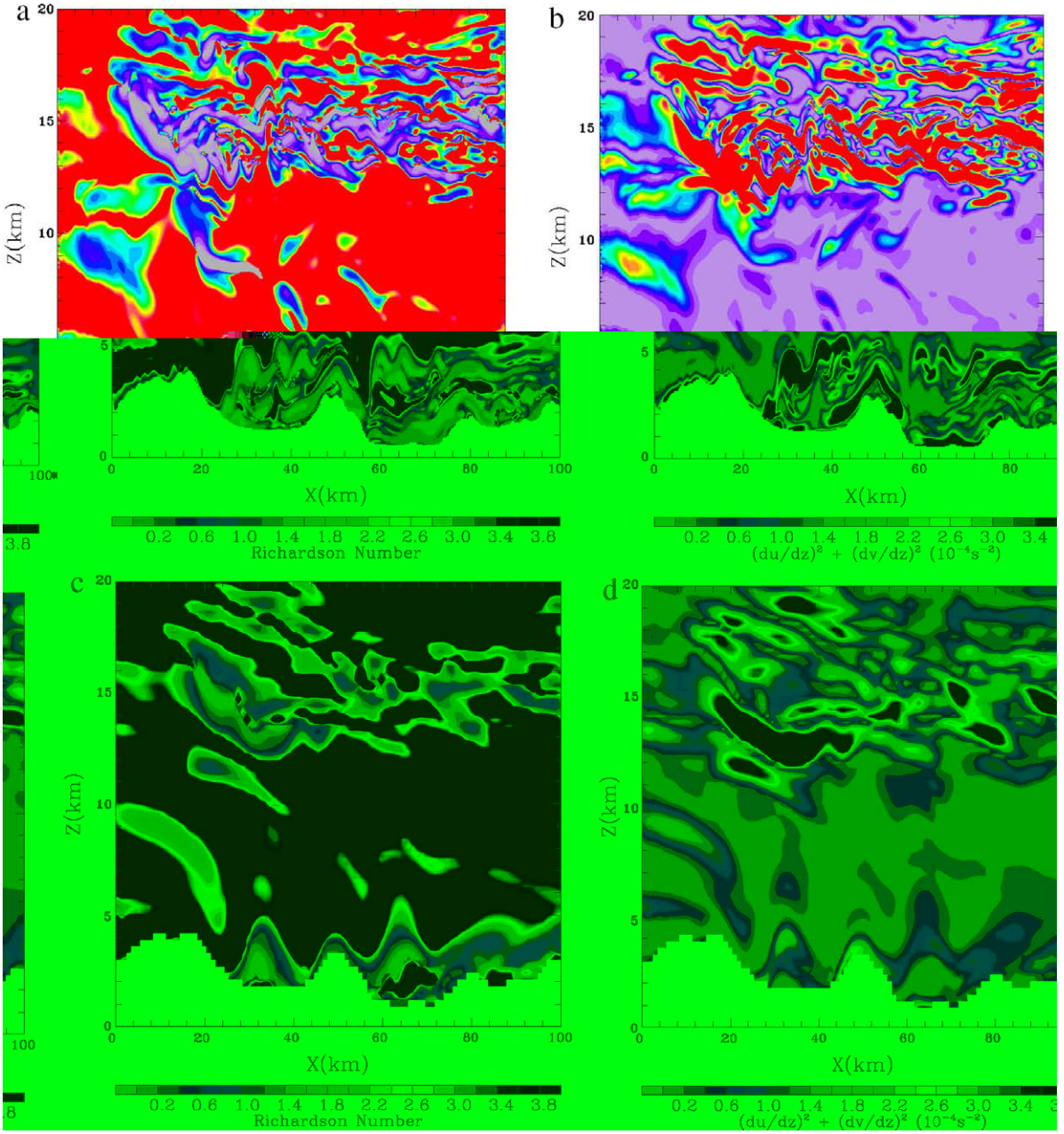

Fig. 9. Longitude–altitude cross-sections from the microscale vertically and horizontally nested domain: (a) Richardson number and (b) shear. (c) and (d) are the same as (a) and (b) but from the finest WRF nest. The time is April 1, 2006 at 8:00 UTC.

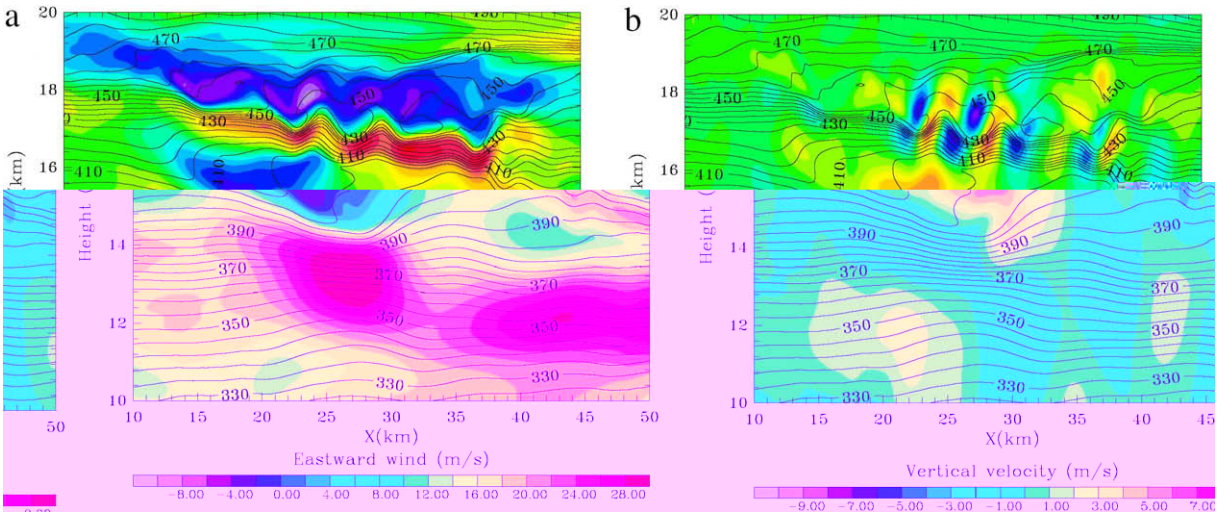

Fig. 10. Longitude–altitude cross-sections for: (a) potential temperature (contour) and eastward wind (color); and (b) potential temperature (contour) and vertical velocity from the microscale nest. The time is 6:40 UTC, April 1, 2006.

small-scale fluctuations that are generated locally since they are not observed at lower levels. The velocity and potential temperature fields show strong inhomogeneities in stratification and shear. High local shear develops at the interface between strong and weak stratification regions. This nonhomogeneous strong shear layer combined with low stratification just above the belt of well packed isentropes locally reduces the Richardson number. As a result, secondary small-scale Kelvin–Helmholtz type instabilities develop locally. They give rise to local overturning just above the high stratification layer. Our microscale simulations are able to resolve these complex multiscale phenomena in the UTLS region.

5. Summary and conclusion

In this paper we presented coupled WRF mesoscale/microscale model with vertical nesting. Vertical nesting is implemented by coupling the higher resolution nest of WRF with a sequence of microscale nests, with increased resolution in both the horizontal and the vertical, and refined vertical gridding to better resolve thin adiabatic layers and sharp gradients that develop near the tropopause and in the lower stratosphere. Fields are relaxed within relaxation zones at both upper and lateral boundaries to values interpolated from the finest WRF nest fields. The vertically relaxed upper boundary conditions prevent the formation of spurious wave reflection at the top of the domain.

The microscale code solves the 3D fully compressible nonhydrostatic equations for atmospheric dynamics with a particular emphasis on improved multiscale resolution of physical processes in the UTLS region. These equations are cast in conservative form and are formulated using a Terrain-following pressure coordinate. The main difference in these equations with respect to those used in WRF is the introduction of a coupled inverse density with the mass of dry air in the column. This results in a different formulation of the equations, and in particular the pressure gradients terms in the momentum equations. By introducing this change, the number of arithmetic operations required for the pressure gradient evaluations in the horizontal momentum equations is reduced by 20%. This formulation also results in linearized gas law that does not include the perturbations of the mass of dry air column.

A new relaxation technique is presented where all fields in the nested domain are relaxed in both the horizontal and the vertical to values interpolated in time and space from the coarse grid domain. The relaxation is implemented as implicit corrections in the acoustic time step. Simulations for idealized cases are conducted to test performance of our proposed relaxation method. The results are compared with the relaxation used in WRF. These tests demonstrate that the implicit relaxation is very effective and robust.

The performance of our model is tested in several cases including mountain wave generation, moist deep convection and the widely used nonlinear density current benchmark. The ability of vertical nesting to improve the numerical solution is demonstrated by conducting a large domain simulation with coarse resolution, a simulation that is nested in the horizontal only, and a simulation that is nested in both the horizontal and the vertical. In this case, horizontal nesting alone was not sufficient to achieve a converged solution. By keeping the same horizontal gridding, and refining the vertical resolution, a converged solution was computed.

The application of microscale vertical nesting is shown in real case simulations of the TREX campaign of measurements where observations have indicated extreme events taking place near the tropopause and in the lower stratosphere. They are characterized by strongly nonlinear interactions and are associated with high activity of mountain waves entering the stratosphere, and formation of small-scale laminated structures. Effective resolution of multiscale dynamics in the UTLS region

requires vertical resolutions that are higher than those typically used in NWP models. In our vertically nested approach, 450 points with improved grid spacing in the UTLS region are used in the vertical, which was never achieved before for real case NWP simulations. Our simulations with refined microscale nests fully resolve sharp adiabatic layers. In regions between these layers, we evidence thin layers with high stratification. They were observed in the UTLS region during the TREX experiment.

The real case coupled WRF mesoscale/microscale simulations presented in this study are conducted for 48 h of physical time. The microscale code run for 3 h covering TREX campaign observational period in the UTLS. The combined computational time of both simulations in a platform using 512 processors is less than 48 h. Thus, these simulations could be conducted in real time forecasting. The computational time could be even faster if the number of vertical levels used in WRF is reduced to a typical operational NWP setups (~ 50), with a refined vertical grid in the microscale code (~ 150). A large speedup can also be achieved if WRF and the microscale codes run in a concurrent mode. This will eliminate the large slow down caused by the frequent input/output required when these two codes run separately.

Acknowledgments

We are grateful to Dr. W. C. Skamarock (NCAR) for his helpful suggestions on this manuscript. We also thank the two anonymous referees for their valuable comments and suggestions, and the WRF group at NCAR for providing the WRF code. This work is sponsored by AFOSR Contract FA9550-08-1-0055 and DoD HPCMPO Challenge Program.

Appendix A. Computational benchmarks

The nonlinear density current benchmark described in [9] is widely used to evaluate the dynamical solvers in nonhydrostatic atmospheric models [1,3]. The computation is initialized for neutral stratification at rest by setting a constant potential temperature of 300 K and by prescribing zero wind velocities. A cold bubble of $\delta\theta(x,z)$ is placed at region centered at 3 km in the vertical using the following relation: $\delta\theta = 0$ if $A > 1$ and $\delta\theta = -15\left\{\frac{\cos(\pi A)+1}{2}\right\}$ if $A < 1$. Here $x_c = 0, z_c = 3$ km, $x_r = 4$ km, $z_r = 2$ km. The eddy diffusivity and the eddy viscosity are taken to be constant with a value of $K = 75$ m^2 s^{-1} in both the momentum equation and potential temperature equations. The following simulations are conducted for 900 s

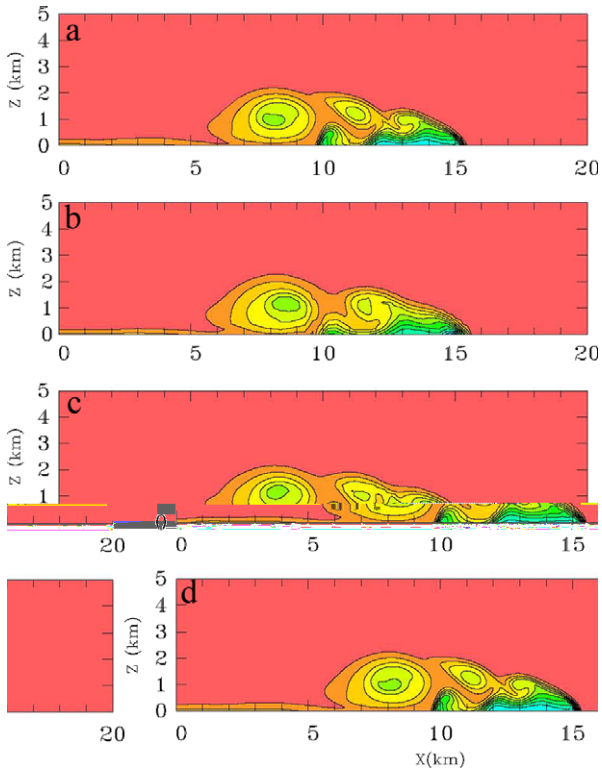

Fig. 11. Nonlinear density current test case: (a) high resolution large domain control simulation with $\delta x = 100$ m and 97 vertical levels, (b) large domain coarse grid simulation with $\delta x = 300$ m and 33 levels, (c) nested domain in the horizontal with $\delta x = 100$ m and 33 levels and (d) horizontally and vertically nested simulation with $\delta x = 100$ m and 97 levels. The parent domain for the nests in (c) and (d) is the coarse domain shown in (b). The time is 900 s.

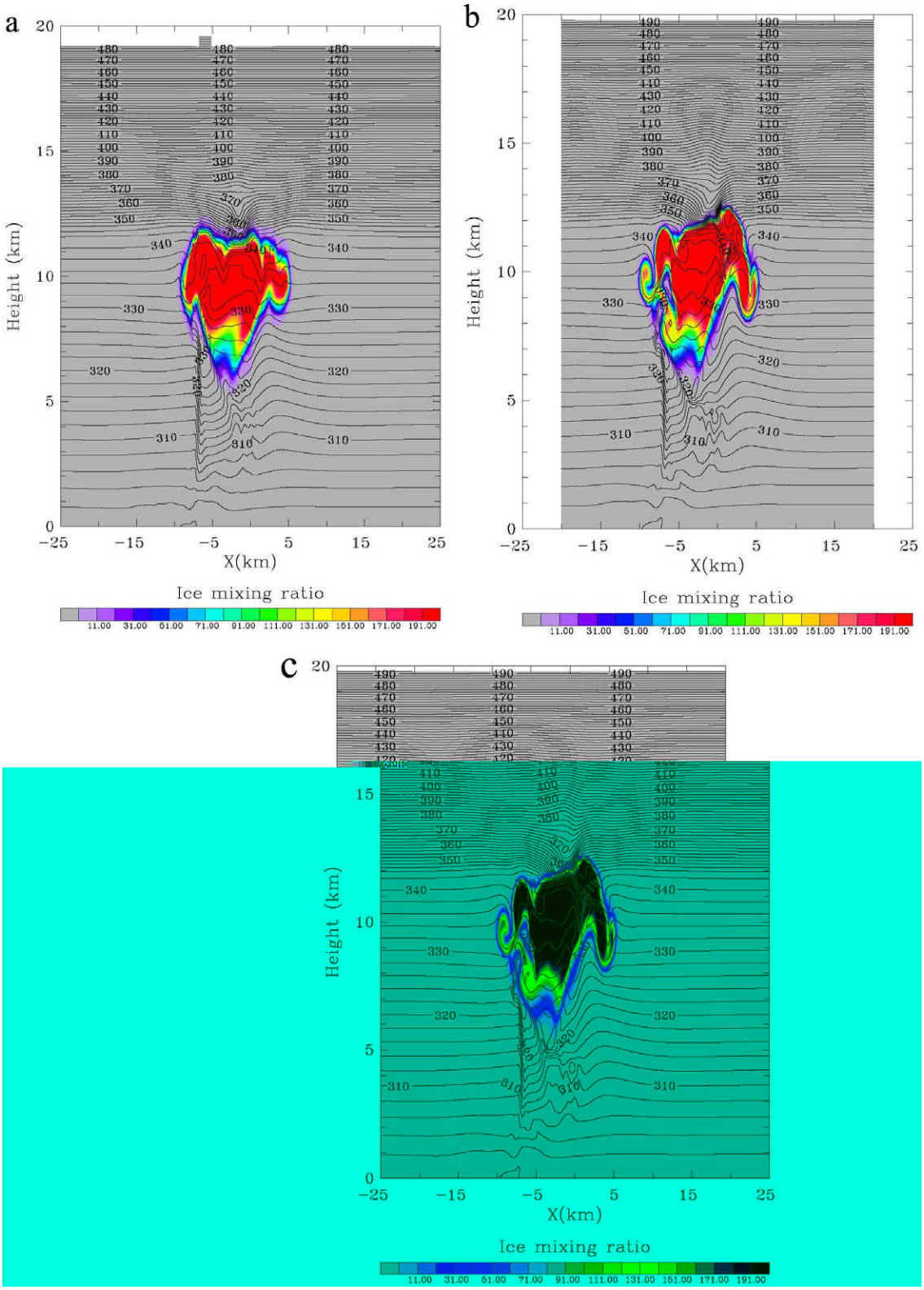

Fig. 12. Vertical cross-sections after 650 time steps from idealized moist deep convection simulation showing potential temperature (contour) and ice cloud (10^{-6} kg/kg, color): (a) from the large domain using 51 vertical levels, (b) from vertically nested domain using 151 vertical levels, and (c) from large domain using high vertical resolution everywhere.

in physical time. Fig. 11(a) shows the converged solution from a control simulation using high resolution everywhere. The horizontal grid spacing is $\delta x = 100$ m and 97 levels are used in the vertical. The pressure at the top is chosen so that the vertical extent of the domain is $z_{top} = 6.4$ km, and the horizontal width is [−46 km, 46 km]. The fields in Fig. 11(a) are plotted between $x = 0$ and $x = 20$ km only for comparison with previous studies. The result shown in Fig. 11(a) is identical to the expected and converged solution [1,3,9]. Fig. 11(b) shows the solution computed with a coarser horizontal ($\delta x = 300$ m) and vertical (33 levels) resolutions. The horizontal and the vertical widths are the same as in Fig. 11(a). The low resolution results in the degradation of the solution. Fig. 11(c) shows the solution computed using nesting in the horizontal direction only. The grid spacing for this nest is $\delta x = 100$ m as in the control simulation, and the horizontal width of the nest is [−30 km, 30 km]. The horizontally nested solution (Fig. 11(c)) shows improvements compared to the parent solution (Fig. 11(b)). However, this solution did not converge yet to the control solution (Fig. 11(a)), even if the nested and the control solution use the same high horizontal resolution ($\delta x = 100$ m). Fig. 11(d) shows a solution obtained using a domain that is nested in both the horizontal and the vertical. The nest is the same as the one used in Fig. 11(c), but, the vertical resolution is increased by a factor of three. The solution has now converged to the control solution (Fig. 11(a). The above results demonstrate that increasing the horizontal resolution alone in a nested simulation may not be sufficient to achieve accurate solutions, and that vertical nesting improves the accuracy of the solutions.

Our benchmark simulations in the moist deep convection test case use the Thompson microphysics parametrization scheme [10]. This scheme has seven water categories including ice cloud. The simulations are initialized with a thermodynamic profile that is close to saturation, and convection is initiated with a three-dimensional temperature perturbation $\delta\theta(x,y,z)$ placed near the lower boundary of the domain using the following relation: $\delta\theta = 0$ if $A > 1$ and $\delta\theta = 3cos^2(0.5\pi A)$ if $A < 1$, where $A = \left\{ \left(\frac{x-x_c}{x_r}\right)^2 + \left(\frac{x-x_c}{x_r}\right)^2 + \left(\frac{z-z_c}{z_r}\right)^2 \right\}^{1/2}$. Here $x_c = 0, y_c = 0, z_c = 1.5$ km, $x_r = 4$ km, $z_r = 1.5$ km. A large domain simulation is conducted using the microscale code with horizontal grid spacing of $\delta x = \delta y = 250$ m, and a coarse grid resolution in the vertical with 51 vertical levels. The pressure at the top is $P_{top} = 57$ mb (about $z = 20$ km). The distribution of the vertical levels is nearly uniform in z-coordinate, and the number of the grid points is $(202 \times 202 \times 51)$. The simulation is conducted for 650 time steps ($\delta t = 2$ s). Fig. 12(a) shows vertical cross-sections of potential temperature and ice cloud from a three-dimensional squall-line simulation of deep moist convection. The structures of the cloud and isentropes resemble those expected from deep convection simulations (i.e. [11,17]); although in these cases, the squall-line simulations were two-dimensional and the microphysics use the simple Kesler scheme that include vapor, cloud and rain only. The fields simulated in the above numerical experiment are archived for each time step, and a second simulation in limited domain is conducted using the microscale code with increased vertical resolution (151 vertical levels). All the fields including water categories are relaxed to the coarse grid fields after interpolation to the nested domain. Fig. 12(b) shows cross-section of potential temperature and ice cloud at the same time as in Fig. 12(a), but from the vertically nested simulation. In order to test the effect of the vertical resolution, the horizontal grid spacing in the nested domain is not changed. Comparison between the fields in Fig. 12(a) and (b) shows similar "large" scale structures. The vertically nested simulation shows more details with small-scale filaments developing near the base of the cloud, which are not present in the coarser case (Fig. 12(a)). To demonstrate that these filaments resolved in the nested domain are not artifacts due to the nesting or to the relaxation, a third simulation is conducted using the same large domain as in the coarse grid case (Fig. 12(a)), but with high vertical resolution everywhere (151 vertical levels). The results from this simulation are plotted in Fig. 12(c). The fields presented in this figure are the same as those shown in Fig. 12(b), with similar fine structures resolved in both cases. This shows that the filaments resolved in the vertically nested domain are not artifacts due to nesting or to the relaxation. The above simulations demonstrate that vertical nesting improves the resolutions of physical processes with finer scales.

References

[1] W.C. Skamarock, J.B. Klemp, A time-split nonhydrostatic atmospheric model for weather research and forecasting applications, J. Comp. Phys. 227 (2008) 3465–3485.
[2] R. Laprise, The Euler equations of motion with hydrostatic pressure as an independant variable, Mon. Wea. Rev. (1992) 197–207.
[3] L.J. Wicker, W.C. Skamarock, Time splitting methods for elastic models using forward time schemes, Mon. Wea. Rev. 130 (2002) 2088–2097.
[4] H.C. Davies, R. Turner, Updating prediction models by dynamical relaxation: an examination of the technique, Quart. J. Roy. Meteor. Soc. 103 (1977) 225–245.
[5] H.C. Davies, Limitations of some common lateral boundary schemes used in regional NWP models, Mon. Wea. Rev. 111 (1983) 1002–1012.
[6] R. Lehmann, On the choice of relaxation coefficients for Davies lateral boundary scheme for regional weather prediction models, Meteor. Atmos. Phys. 52 (1993) 1–14.
[7] P. Marbaix, H. Gallee, O. Brasseur, J.P. Van Ypersele, Lateral boundary conditions in regional climate models: a detailed study of the relaxation procedure, Mon. Wea. Rev. 111 (2003) 461–479.
[8] J.B. Klemp, J. Dudhia, A. Hassiotis, An upper gravity wave absorbing layer for NWP applications, Mon. Wea. Rev. 136 (2008) 3987–4004.
[9] J.M. Straka, R.B. Wilhelmson, L.J. Wicker, J.R. Anderson, K.K. Droegemeier, Numerical solutions of a non-linear density current: a benchmark solution and comparisons, Int. J. Numer. Method Fluid 17 (1993) 1–22.
[10] G. Thompson, R.M. Rasmussen, K. Manning, Explicit forecasts of winter precipitation using an improved bulk microphysics scheme. Part 1: description and sensitivity analysis, Mon. Wea. Rev. 132 (2004) 519–542.
[11] B. Potter, J.R. Holton, The role of monsoon convection in the dehydration of the lower tropical stratosphere, J. Atmos. Sci. 52 (1995) 1034–1050.
[12] D.L. Williamson, P.J. Rasch, Two-dimensional semi-Lagrangian transport with shape preserving interpolation, Mon. Wea. Rev. 117 (1989) 102–129.
[13] B. Joseph, A. Mahalov, B. Nicolaenko, K.L. Tse, Variability of turbulence and its outer scales in a nonuniformly stratified tropopause jet, J. Atmos. Sci. 41 (2004) 524–537.

[14] V. Grubisic, J.D. Doyle, J. Kuettner, S. Mobbs, R.B. Smith, D. Whitman, R. Dirks, S. Czyzyk, S.A. Cohn, S. Vosper, M. Weissmann, S. Haimov, S. De Wekker, L.L. Pan, F.K. Chow, The Terrain-induced rotor experiment: an overview of the field campaign and some highlights of special observations, Mon. Wea. Rev. (in press).
[15] K.L. Tse, A. Mahalov, B. Nicolaenko, H.J.S. Fernando, Quasi-equilibrium dynamics of shear-stratified turbulence in a model tropospheric jet, J. Fluid Mech. 496 (2003) 73–103.
[16] H. Teitelbaum, M. Moustaoui, C. Basdevant, J.R. Holton, An alternative mechanism explaining the hygropause formation in tropical regions, Geophys. Res. Lett. 27 (2000) 221–224.
[17] M. Moustaoui, B. Joseph, H. Teitelbaum, Mixing layer formation near the tropopause due to gravity wave-critical level interactions in a cloud-resolving model, J. Atmos. Sci. 61 (2004) 3112–3124.
[18] P.K. Smolarkiewicz, G.A. Grell, A class of monotone interpolation schemes, J. Comp. Phys. 101 (1992) 431–440.
[19] G.S. Dietachmayer, K.K. Droegemeier, Application of continuous dynamic grid adaptation techniques to meteorological modeling, Part I: basic formulation and accuracy, Mon. Wea. Rev. 120 (1992) 1675–1706.
[20] W.C. Skamarock, J.B. Klemp, Adaptive grid refinement for two-dimensional and three-dimensional nonhydrostatic atmospheric flow, Mon. Wea. Rev. 121 (1993) 788–804.
[21] J. Behrens, Adaptive atmospheric modeling: scientific computing at its best, Comput. Sci. Eng. 7 (2005) 76–83.
[22] J. Dudhia, A nonhydrostatic version of the Penn State NCAR mesoscale model: validation tests and simulation of an Atlantic cyclone and cold front, Mon. Wea. Rev. 121 (1993) 1493–1513.
[23] R.M. Hodur, The naval research laboratory's coupled ocean/atmosphere mesoscale prediction system (COAMPS), Mon. Wea. Rev. 125 (1997) 1414–1430.
[24] A. Shchepetkin, J.C. McWilliams, Regional ocean model system: a split-explicit ocean model with a free surface and topography-following vertical coordinate, Ocean Model. 9 (2005) 347–404.
[25] P. Oddo, N. Pinardi, Lateral open boundary conditions for nested limited area models: a scale selective approach, Ocean Model. 10 (2008) 134–156.